The Astronomical Journal, 167:154 (13pp), 2024 April https://doi.org/10.3847/1538-3881/ad2703

OGLE-2014-BLG-0221Lb: A Jupiter Mass Ratio Companion Orbiting Either a Late-type Star or a Stellar Remnant

Rintaro Kirikawa[1,17], Takahiro Sumi[1,17], David P. Bennett[2,3,17], Daisuke Suzuki[1,17], Naoki Koshimoto[1,17], Shota Miyazaki[4,17], Ian A. Bond[5,17], Andrzej Udalski[6,18], Nicholas J. Rattenbury[7,17]
(Leading Authors),
Fumio Abe[8], Richard Barry[2], Aparna Bhattacharya[2,3], Hirosane Fujii[1], Akihiko Fukui[9,10], Ryusei Hamada[1], Yuki Hirao[11], Stela Ishitani Silva[2,12], Yoshitaka Itow[8], Yutaka Matsubara[8], Yasushi Muraki[8], Greg Olmschenk[2], Clément Ranc[13], Yuki K. Satoh[14], Mio Tomoyoshi[1], Paul . J. Tristram[15], Aikaterini Vandorou[2,3], Hibiki Yama[1], Kansuke Yamashita[1]
(MOA COLLABORATION),
and
Przemek Mróz[6], Radosław Poleski[6], Jan Skowron[6], Michał K. Szymański[6], Igor Soszyński[6], Paweł Pietrukowicz[6], Szymon Kozłowski[6], Krzysztof Ulaczyk[6,16], and Mateusz J. Mróz[6]
(OGLE COLLABORATION)

[1] Department of Earth and Space Science, Graduate School of Science, Osaka University, Toyonaka, Osaka 560-0043, Japan
[2] Code 667, NASA Goddard Space Flight Center, Greenbelt, MD 20771, USA
[3] Department of Astronomy, University of Maryland, College Park, MD 20742, USA
[4] Institute of Space and Astronautical Science, Japan Aerospace Exploration Agency, 3-1-1 Yoshinodai, Chuo, Sagamihara, Kanagawa 252-5210, Japan
[5] Institute of Natural and Mathematical Sciences, Massey University, Auckland 0745, New Zealand
[6] Warsaw University Observatory, Al. Ujazdowskie 4, 00-478 Warszawa, Poland
[7] Department of Physics, University of Auckland, Private Bag 92019, Auckland, New Zealand
[8] Institute for Space-Earth Environmental Research, Nagoya University, Nagoya 464-8601, Japan
[9] Department of Earth and Planetary Science, Graduate School of Science, The University of Tokyo, 7-3-1 Hongo, Bunkyo-ku, Tokyo 113-0033, Japan
[10] Instituto de Astrofísica de Canarias, Vía Láctea s/n, E-38205 La Laguna, Tenerife, Spain
[11] Institute of Astronomy, Graduate School of Science, The University of Tokyo, 2-21-1 Osawa, Mitaka, Tokyo 181-0015, Japan
[12] Department of Physics, The Catholic University of America, Washington, DC 20064, USA
[13] Sorbonne Université, CNRS, UMR 7095, Institut d'Astrophysique de Paris, 98 bis bd Arago, 75014 Paris, France
[14] College of Science and Engineering, Kanto Gakuin University, 1-50-1 Mutsuurahigashi, Kanazawa-ku, Yokohama, Kanagawa 236-8501, Japan
[15] University of Canterbury Mt. John Observatory, P.O. Box 56, Lake Tekapo 8770, New Zealand
[16] Department of Physics, University of Warwick, Gibbet Hill Road, Coventry, CV4 7AL, UK
Received 2023 October 16; revised 2024 January 3; accepted 2024 January 9; published 2024 March 14

Abstract

We present the analysis of the microlensing event OGLE-2014-BLG-0221, a planetary candidate event discovered in 2014. The photometric light curve is best described by a binary-lens single-source model. Our light-curve modeling finds two degenerate models, with event timescales of $t_{\rm E} \sim 70$ days and $\sim$110 days. These timescales are relatively long, indicating that the discovered system would possess a substantial mass. The two models are similar in their planetary parameters with a Jupiter mass ratio of $q \sim 10^{-3}$ and a separation of $s \sim 1.1$. Bayesian inference is used to estimate the physical parameters of the lens, revealing that the shorter timescale model predicts 65% and 25% probabilities of a late-type star and white dwarf host, respectively, while the longer timescale model favors a black hole host with a probability ranging from 60% to 95%, under the assumption that stars and stellar remnants have equal probabilities of hosting companions with planetary mass ratios. If the lens is a remnant, this would be the second planet found by microlensing around a stellar remnant. The current separation between the source and lens stars is 41–139 mas depending on the models. This indicates the event is now ready for high-angular-resolution follow-up observations to rule out either of the models. If precise astrometric measurements are conducted in multiple bands, the centroid shift due to the color difference between the source and lens would be detected in the luminous lens scenario.

Unified Astronomy Thesaurus concepts: Gravitational microlensing (672); Exoplanets (498); Stellar remnants (1627)

Supporting material: data behind figure

1. Introduction

Gravitational microlensing is a well-known method for the discovery of exoplanets. Since the first discovery of a planet via microlensing in 2004 (Bond et al. 2004; Bennett et al. 2006), the number of exoplanets detected by microlensing has grown to 200 (Akeson et al. 2013). The most likely lens star in a microlensing event is a low-mass late-type star as these are the most prolific in our galaxy. A large fraction of planets

[17] MOA collaboration.
[18] OGLE collaboration.

discovered by microlensing are gas giants.[19] Such planets are less likely to be formed around low-mass stars according to the core accretion model of planet formation (Ida & Lin 2005; Burn et al. 2021). Suzuki et al. (2016) gave a statistical analysis of the set of microlensing planets and found the planet–star mass ratio function was best characterized by a broken power law with the break at $q = 1.7 \times 10^{-4}$, which corresponds to the mass of Neptune. Comparison of the result to population synthesis models of the core accretion admitted excess in the microlensing planet beyond $q \sim 10^{-4}$ (Suzuki et al. 2018), including a gas giant mass ratio regime.

Microlensing surveys were originally initiated to search for dark matter in the form of MAssive Compact Halo Objects (MACHOs; Paczynski 1986) in which stellar remnants, substellar objects, and planets are the expected populations. Identifying isolated black holes (BHs) as a part of a population of MACHOs was not successful until recently owing to the degeneracy in mass and distance present in the interpretation of most single-lens events. The first definitive detection of an isolated BH was made possible through observations of the astrometric shift of the apparent source position using high-resolution imaging of the Hubble Space Telescope (Lam et al. 2022; Mróz et al. 2022; Sahu et al. 2022).

The first detection of a stellar remnant by microlensing was made in 2021 (Blackman et al. 2021). Following the actual discovery in 2010 (Bachelet et al. 2012), follow-up observations with high-resolution imaging using the Keck II telescope were conducted to resolve the source and lens and resulted in no detection of a luminous lens. The lens system was concluded to be composed of a white dwarf (WD) and an accompanying Jovian planet.

So far, these are the only examples of stellar remnants found by microlensing while there are a few more candidates to be confirmed (e.g., Miyake et al. 2012; Shvartzvald et al. 2015). An ambitious program with the Nancy Grace Roman Space Telescope, NASA's next flagship mission (Spergel et al. 2015), has been proposed to detect isolated BHs, utilizing Roman's high-precision photometry and astrometry (Lam et al. 2023). The survey strategy required for the detection of isolated BHs is mostly satisfied by the notional design of the Galactic Bulge Time Domain Survey optimized for the detection of exoplanets toward the Galactic bulge. Lam et al. (2023) predicted more than 300 isolated BH detections among which 270 BHs can be characterized by additional daily cadence observations and an astrometric precision of 0.1 mas. The same strategy should also enable the discovery of BH binaries. These are less common but more likely to be characterized with additional constraints on the mass–distance degeneracy from accurate measurement of a projected source size. A future BH survey using the powerful capability of Roman seems promising; however, we need to wait until its expected launch in 2026. A discussion now of the discoveries of BHs and other compact objects is important for establishing the future prospects of such a survey.

This paper presents an analysis of the microlensing event OGLE-2014-BLG-0221. Section 2 describes how the event was discovered and observed. Section 3 gives the details of our light-curve analysis. In Section 4, we investigate the source property using a color–magnitude diagram for field stars around the event coordinate. The lens properties are estimated in Section 5. Then, we discuss the results in Section 6.

[19] 110 discovered microlensing planets have estimated masses larger than that of Saturn (Akeson et al. 2013). Note that microlensing has higher detection efficiency for higher mass ratio planets.

2. Observation

Microlensing event OGLE-2014-BLG-0221 was detected by the Optical Gravitational Lensing Experiment (OGLE; Udalski et al. 2015) collaboration on 2014 March 6 (HJD′ ≡ HJD − 2450000 ∼ 6723) as a part of the OGLE-IV survey. The OGLE group conducted the observations with their 1.3 m Warsaw telescope at the Las Campanas Observatory in Chile. The event coordinate was first reported at $(\mathrm{R.A.}, \mathrm{decl.})_{\mathrm{J2000}} = (18^{\mathrm{h}}01^{\mathrm{m}}12\overset{\mathrm{s}}{.}90, -27°25'37\overset{''}{.}2)$, corresponding to Galactic coordinates $(l, b) = (3.044660, -2.195338)$, where a known faint star is located; however, later, a centroid shift of the lensed source was observed while the source was magnified. The coordinate was corrected to $(\mathrm{R.A.}, \mathrm{decl.})_{\mathrm{J2000}} = (18^{\mathrm{h}}01^{\mathrm{m}}12\overset{\mathrm{s}}{.}90, -27°25'36\overset{''}{.}35)$, corresponding to Galactic coordinates $(l, b) = (3.044658, -2.195316)$, and the event was reidentified by the New Objects in the OGLE Sky (NOOS) system (Udalski 2003) as the lensing of a previously unknown object and redesignated as OGLE-2014-BLG-0284. OGLE-2014-BLG-0221 was located in the OGLE field BLG511 and was detected using a nominal cadence of every 60 minutes for their *I*-band observations.

The event was also independently discovered by the Microlensing Observations in Astrophysics (MOA; Bond et al. 2001; Sumi et al. 2003) collaboration as a part of the MOA-II survey on 2014 March 9 and designated as MOA-2014-BLG-069. The event was located in MOA field gb10. This field was observed in the survey with a cadence of 15 minutes. The MOA group uses their 1.8 m MOA-II telescope and 2.2 deg^2 wide field-of-view camera, MOA-cam3, at the Mount John Observatory in New Zealand (Sako et al. 2008).

The OGLE photometric data were obtained mostly in the standard Kron–Cousins *I* band and occasionally in the standard Johnson *V* band in order to extract color information of the source star. The MOA photometric data were obtained in the designated MOA-Red band, equivalent to a combined band of the standard Cousins *R* and *I*. MOA also occasionally observes in the Johnson *V* band; however, unfortunately, no data were taken in 2014. OGLE and MOA reduced the data with their own pipelines (Bond et al. 2001; Udalski 2003) based on their implementation of the difference image analysis method (Alard & Lupton 1998).

The pipelines often underestimate uncertainties of photometric data for a stellar dense region. For this reason, we rescaled the errors to account for low-level unknown systematics so that the reduced χ^2 (or $\chi^2/\mathrm{d.o.f.}$) equals 1, following the standard procedure detailed in (Bennett et al. 2008; Yee et al. 2012). The rescaling formula is

$$\sigma'_i = k\sqrt{\sigma_i^2 + e_{\mathrm{min}}^2}\,, \tag{1}$$

where σ'_i is the rescaled error, σ_i is the error before rescaling, and k and e_{min}^2 are the rescaling parameters. Data sets and rescaling parameters adopted in the analysis are listed in Table 1. We used the optimized photometry of OGLE-2014-BLG-0221 for OGLE data.

3. Light-curve Analysis

The light curve of OGLE-2014-BLG-0221 in Figure 1 shows a clear anomaly from HJD′ ∼6738 to 6746, a deviation from

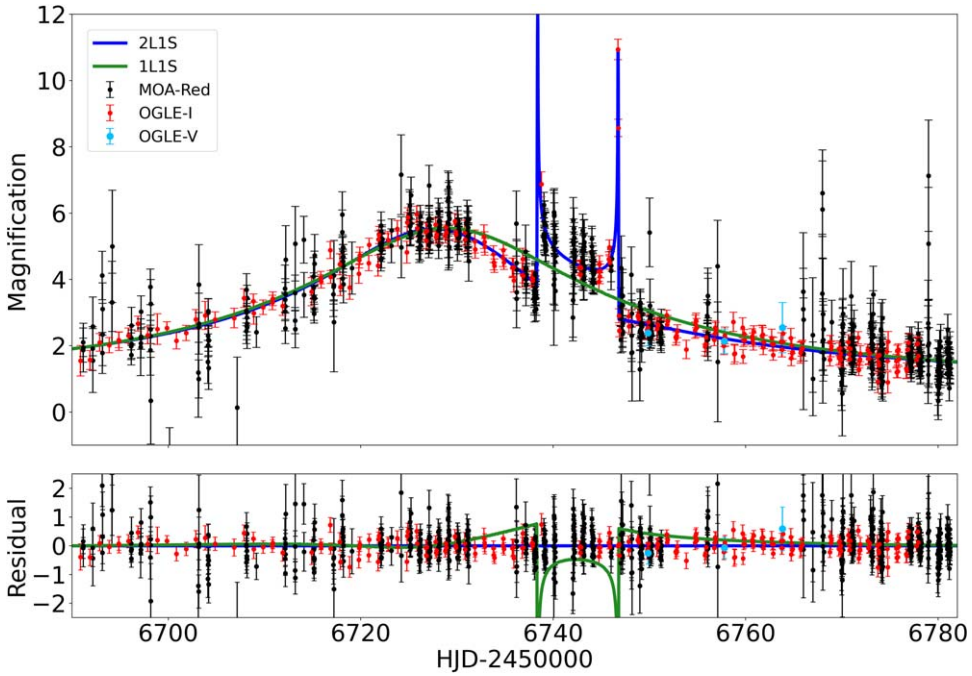

Figure 1. Light curve of OGLE-2014-BLG-0221. The black, red, and light-blue data points are the reduced photometric data from the MOA-Red and OGLE *I*- and *V*-band observations, respectively. The blue and green lines represent the best-fit binary-lens single-source model and best-fit single-lens single-source model. The lower panel shows the residuals from the best-fit binary-lens model.

(The data used to create this figure are available.)

Table 1
Data Set and Rescaling Parameters

Name	Telescope	Filter	$N_{\rm data}$[a]	k[b]	$e_{\rm min}$[b]
OGLE	Warsaw 1.3 m	I	2480	1.575	0
		V	205	1.336	0.003
MOA	MOA-I I 1.8 m	MOA-Red	7835	0.974	0.026

Notes.
[a] The number of data points.
[b] The rescaling parameters.

the symmetric Paczynski curve (Paczynski 1986) with a caustic crossing–like shape, indicating the presence of a binary-lens system. We modeled the light curve with the following formularization.

The timescale of the event is defined as

$$t_{\rm E} = \frac{\theta_{\rm E}}{\mu_{\rm rel}}, \tag{2}$$

where $\mu_{\rm rel}$ is the relative source–lens proper motion and

$$\theta_{\rm E} = \sqrt{\kappa M \pi_{\rm rel}}, \tag{3}$$

is the angular Einstein radius as a function of the constant $\kappa = 4G/c^2$, the total lens mass M, and the relative source–lens parallax $\pi_{\rm rel} = (1\ {\rm au})(1/D_{\rm L} - 1/D_{\rm S})$.

The time at the source–lens closest approach and the impact parameter are parameterized as t_0 and u_0. The ratio of the angular source radius θ_* and the angular Einstein radius is also measured as

$$\rho = \frac{\theta_*}{\theta_{\rm E}}. \tag{4}$$

For the case of a binary-lens event, the mass ratio of the primary and companion q, the projected angular separation of them in units of the angular Einstein radius s, and the sky projected source incident angle α relative to the binary-lens axis are included as additional parameters. We considered annual parallax effect and linear-lens orbital motion modeled by two additional parameters for each, ($\pi_{\rm E,N}$, $\pi_{\rm E,E}$) and ($\gamma_\parallel = \frac{ds}{dt}$, $\gamma_\perp = \frac{d\alpha}{dt}$), where $\pi_{\rm E,N}$ and $\pi_{\rm E,E}$ are the north and east components of the microlensing parallax vector (Gould 2004) and $\frac{ds}{dt}$ and $\frac{d\alpha}{dt}$ are the projected linear and angular motions of the lens companion, expressed as the rate of change in s and α, around the primary (Skowron et al. 2011).

As boundary conditions of a gravitationally bound lens companion, we constrain the orbital motion parameters such that the ratio of the projected kinetic to the potential energy of the lens $\left(\frac{\rm KE}{\rm PE}\right)_\perp$ does not go beyond 0.5, under the assumption of a circular orbit (Dong et al. 2009). The source orbital motion, another higher-order effect called xallarap (Poindexter et al. 2005), arising if the source star has a companion, is known to mimic the effects of annual parallax and lens orbital motion. While we also modeled this effect with seven additional parameters ($\xi_{\rm E,N}$, $\xi_{\rm E,E}$, R. A.$_\xi$, decl.$_\xi$, P_ξ, e_ξ, $T_{\rm peri}$), we will not go into detail in this paper as we found no solid evidence for xallarap.

We applied a linear limb-darkening model to the source star in our modeling. With $T_{\rm eff} \sim 5500$ K estimated from the source color (see Section 4) and an assumption of surface gravity

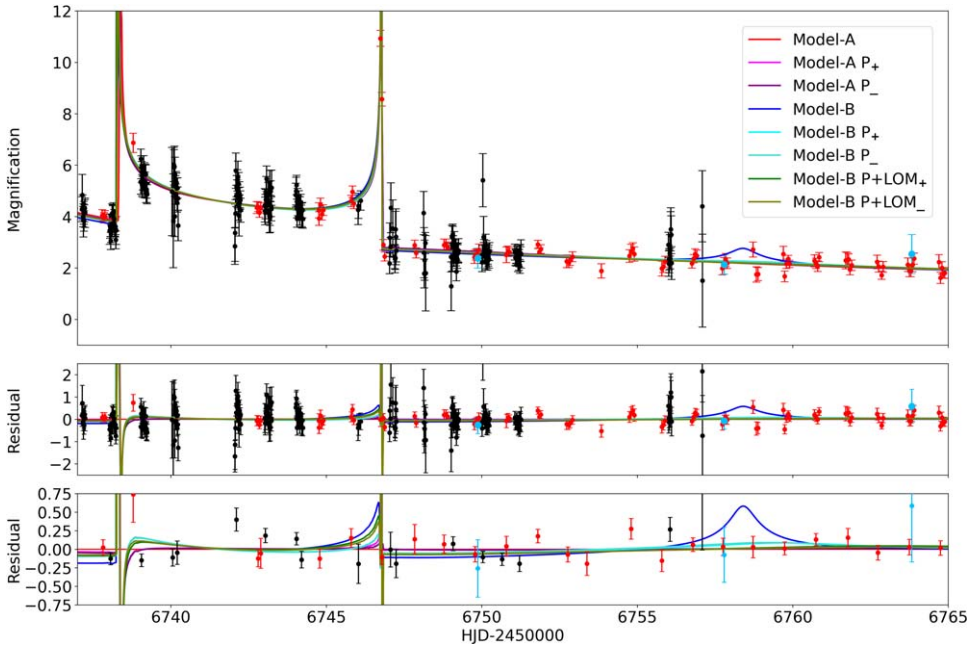

Figure 2. Model light curves of the two degenerate models around the anomaly. Model-A, Model-A $P_{\pm}$, Model-B, Model-B $P_{\pm}$, and Model-B P+LOM$_{\pm}$ are plotted. As different sources and blending fluxes between Model-A and Model-B make different magnifications, the magnification of Model-B is scaled by the source and blending fluxes of Model-A for comparison. The lower residual panel shows the data points binned in 1 day intervals.

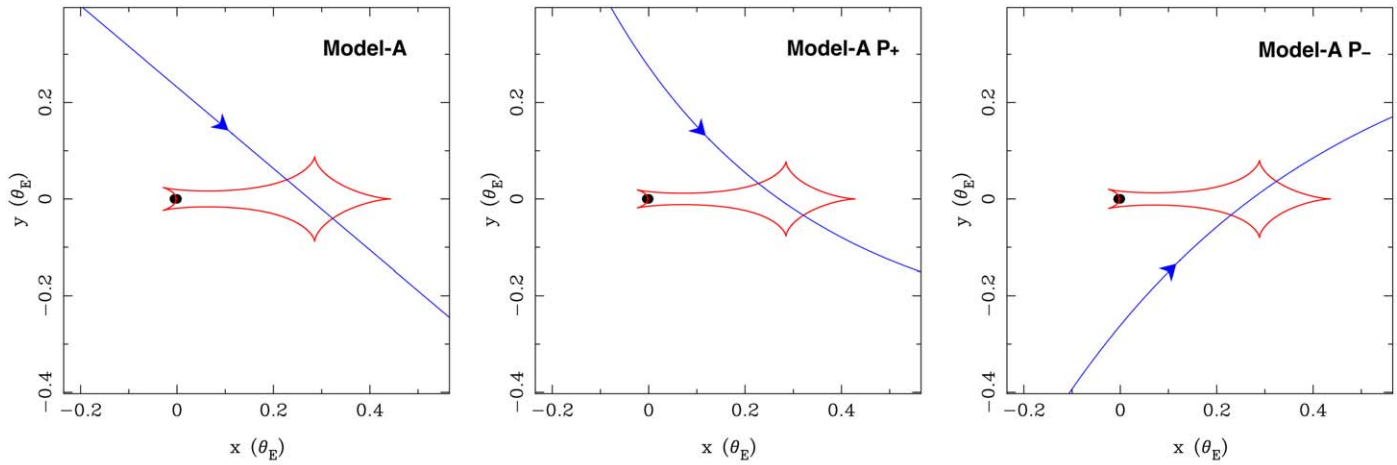

(a) Model-A (b) Model-A P_+ (c) Model-A P_-

Figure 3. Caustic geometry corresponding to Model-A for versions with nonparallax and parallax ($P_{\pm}$). The caustic is shown in the red curved line. The blue line is the source trajectory.

$\log g = 4.5$ cm s^{-2} and solar metallicity $\log[M/H] = 0$, the limb-darkening coefficients $u_I = 0.5189$, $u_V = 0.6854$, and $u_{MOA-Red} = 0.6052$ were determined from the tables of Claret & Bloemen (2011).

We searched for the best-fit binary-lens model by exploring the parameter space using our modeling software (Sumi et al. 2010), which is based on the Markov Chain Monte Carlo method (Verde et al. 2003) and the image-centered ray-shooting method (Bennett & Rhie 1996). In order to explore a wide range of parameter values, we start from a grid search in which we divide the (q, s, α) parameter space into $11 \times 22 \times 40$ uniformly spaced grids with $\log q \in [-4, 0]$, $\log s \in [-0.5, 0.55]$, $\alpha \in [0, 2\pi)$. We search for a best-fit model at each grid by fixing (q, s, α) and allowing other parameters free. Among the 9680 models, 100 models with the lowest χ^2 values are then refined to explore the global minimum by releasing the fixed (q, s, α) to vary. We finally exclude all the models that exceed the threshold of $\Delta\chi^2 = 100$ from the best-fit lowest χ^2 model, through which we find two degenerate models remain.

Figure 2 shows the two degenerate models, Model-A and Model-B, with corresponding geometries of the caustics shown in Figures 3 and 4. The nonparallax, parallax, and parallax plus lens orbital motion (LOM) models are plotted in Figure 2 and denoted by the unmarked model names and the extra characters P and P+LOM, respectively. Subscripts "+" and "−" refer to degenerate parallax models with corresponding signs of the impact parameter u_0. The parameters of the models are listed in Tables 2 and 3.

The event timescales of both Model-A and Model-B, $t_E \sim 70$ days and 110 days, respectively, are longer than the typical

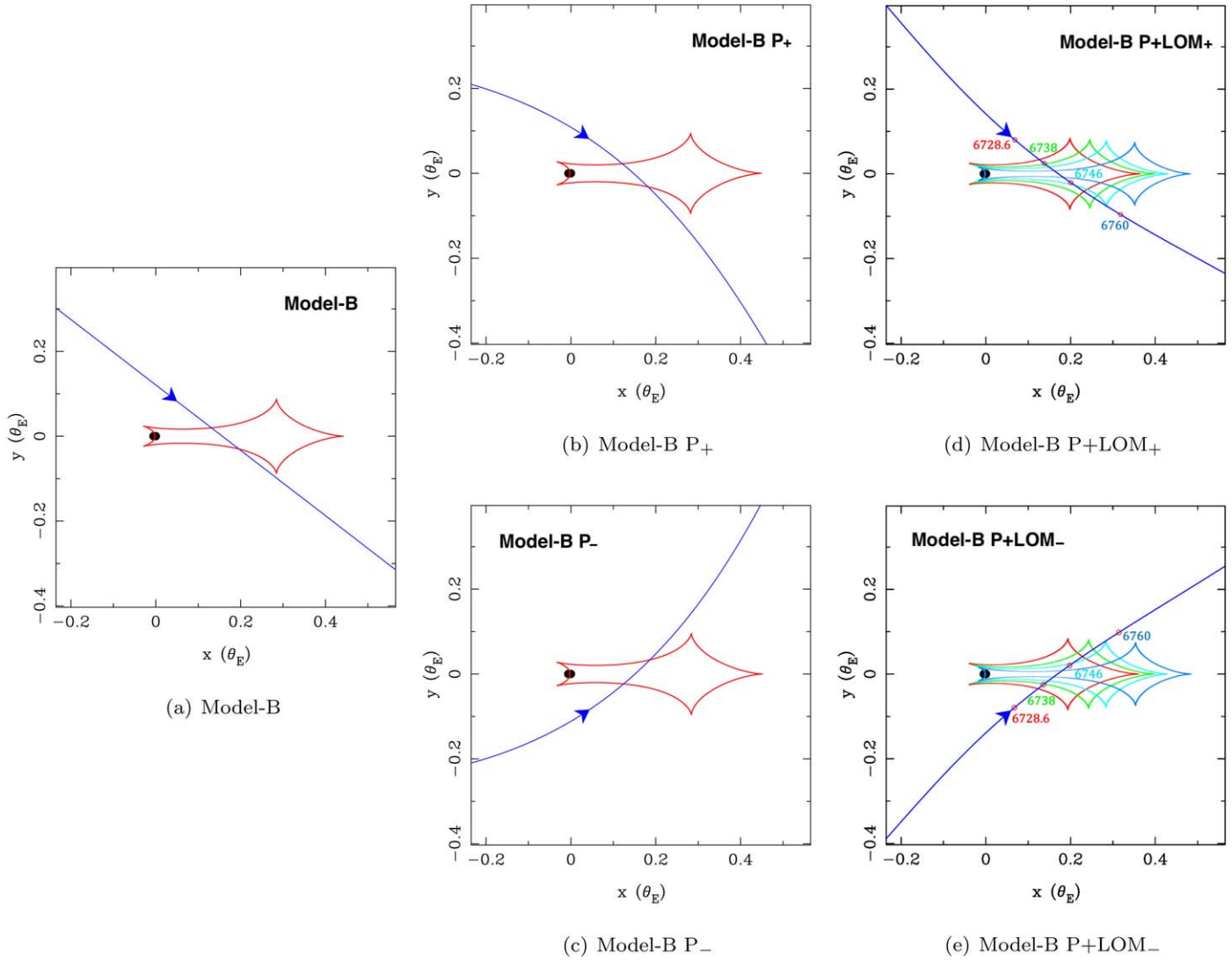

Figure 4. Caustic geometry corresponding to Model-B for versions with nonparallax, parallax ($P_{\pm}$), and parallax plus lens orbital motion ($P+LOM_{\pm}$). The caustics at HJD′ = 6728.6, 6738, 6746, and 6760 are plotted for $P+LOM_{\pm}$ with the instantaneous source positions in the red open circles whose sizes are not in scale.

Table 2
Model-A Parameters

Parameter	Model-A	Model-A P_+	Model-A P_-
t_E (day)	67.6 ± 1.3	73.1 ± 3.0	70.9 ± 2.3
t_0 (HJD′)	6728.34 ± 0.14	6728.20 ± 0.15	6728.17 ± 0.16
u_0	0.1773 ± 0.0038	0.1764 ± 0.0047	-0.1774 ± 0.0039
q (10^{-3})	6.03 ± 0.34	4.64 ± 0.62	5.02 ± 0.54
s	1.1517 ± 0.0049	1.1516 ± 0.0059	1.1538 ± 0.0048
α (rad)	0.701 ± 0.012	0.793 ± 0.030	0.771 ± 0.028
ρ (10^{-4})	7.80 ± 1.54	6.94 ± 1.76	7.08 ± 2.09
$\pi_{E,N}$	⋯	-0.556 ± 0.164	0.431 ± 0.157
$\pi_{E,E}$	⋯	0.100 ± 0.046	0.093 ± 0.045
π_E	⋯	0.565 ± 0.167	0.441 ± 0.160
χ^2	10489.4	10483.5	10486.9
$\Delta\chi^2$	⋯	−5.9	−2.5

Note. Best-fit values with uncertainties corresponding to the 68% credible intervals of the MCMC posterior distributions.

timescale of $t_E \sim 30$ days for events toward the Galactic bulge (Mróz et al. 2019), from which we anticipate a heavy lens. Model-A resembles Model-B in the binary-lens parameters q, s, and α but differs in t_E and ρ. The larger t_E value and the smaller ρ value of Model-B imply a larger θ_E compared to that of Model-A.

The nonparallax model of Model-A already fits well to the light curve, whereas Model-B shows a deviation around HJD′ $\sim$ 6760 due to cusp reapproach after the caustic exit, resulting in $\Delta\chi^2 \sim 45$ between Model-A and Model-B. Once higher-order effects are considered, Model-B significantly improves from the nonparallax model by avoiding the cusp reapproach and $\Delta\chi^2 \sim -60$ and ~ -85 for the parallax and parallax plus LOM models. In contrast, Model-A only improves by $\Delta\chi^2 = -6$, showing no distinct evidence of the parallax signal. Therefore, we conclude that a higher-order effect of either the parallax, lens orbital motion, or xallarap needs to be involved in Model-B but not in Model-A.

In order to take the higher-order effect into account for Model-B, we begin with the parallax alone model that already provides a good fit to the flat feature around HJD′ $\sim$ 6760 and then add LOM for getting more rigorous parallax parameter values and errors. Our modeling suffers a degeneracy known as the ecliptic degeneracy, where light curves with the parameters (u_0, α, $\pi_{E,N}$, $\gamma_\perp$) = − (u_0, α,

Table 3
Model-B Parameters

Parameter	Model-B	Model-B P_+	Model-B P_-	Model-B P+LOM$_+$	Model-B P+LOM$_-$
t_E (day)	104.5 ± 0.3	108.2 ± 3.9	105.3 ± 3.5	109.8 ± 3.5	112.9 ± 2.4
t_0 (HJD′)	6728.63 ± 0.06	6728.92 ± 0.13	6728.92 ± 0.14	6728.64 ± 0.09	6728.59 ± 0.15
u_0	0.0957 ± 0.0003	0.0914 ± 0.0025	-0.0941 ± 0.0039	0.1054 ± 0.0031	-0.1042 ± 0.0015
q (10^{-3})	6.02 ± 0.05	6.96 ± 0.53	7.14 ± 0.30	4.73 ± 0.16	4.74 ± 0.30
s	1.1510 ± 0.0007	1.1496 ± 0.0040	1.1506 ± 0.0024	1.1026 ± 0.0021	1.1000 ± 0.0045
α (rad)	0.656 ± 0.003	0.598 ± 0.022	-0.597 ± 0.006	0.705 ± 0.004	-0.700 ± 0.013
ρ (10^{-4})	0.38 ± 0.15	1.40 ± 0.79	1.44 ± 0.19	0.98 ± 0.17	1.11 ± 0.18
$\pi_{E,N}$	⋯	0.304 ± 0.093	-0.337 ± 0.022	-0.419 ± 0.010	0.390 ± 0.062
$\pi_{E,E}$	⋯	-0.070 ± 0.032	-0.060 ± 0.018	-0.010 ± 0.018	-0.058 ± 0.026
π_E	⋯	0.312 ± 0.085	0.342 ± 0.022	0.419 ± 0.009	0.394 ± 0.059
$\gamma_\parallel$ (yr^{-1})	⋯	⋯	⋯	1.01 ± 0.02	1.05 ± 0.08
$\gamma_\perp$ (rad yr^{-1})	⋯	⋯	⋯	1.35 ± 0.03	-1.36 ± 0.39
χ^2	10534.2	10475.3	10473.5	10449.5	10457.6
$\Delta\chi^2$	⋯	−58.9	−60.7	−84.7	−76.6
$(KE/PE)_\perp$	⋯	⋯	⋯	0.373	0.477

Note. Best-fit values with uncertainties corresponding to the 68% credible intervals of the MCMC posterior distributions.

$\pi_{E,N}$, $\gamma_\perp$) appear nearly identical if the direction of the Sun's acceleration is constant (Skowron et al. 2011). This occurs when a deviation due to parallax is short timescale or the event coordinate is close to the ecliptic plane, which is true for the Galactic bulge. We identify the degenerate models with the subscripts "+" and "−" taken from the sign of u_0. The "+" and "−" models have similar parameter values except for the sign and are indeed indistinguishable from the light curve and χ^2.

The inclusion of LOM improves the fitting by $\Delta\chi^2 \sim -25$ and reduces the uncertainty in the parallax vector from ∼30% to ∼15% in the positive $\pi_{E,N}$ regime and ∼6% to ∼2% in the negative $\pi_{E,N}$ regime, as can be noticed in Tables 2 and 3 and Figure 5 where we show the posterior distribution of the parallax vector components with a uniform prior of $\pi_{E,N}$ and $\pi_{E,E}$. However, we find that $\Delta\chi^2$ mostly comes from the baseline systematics but not from the magnification part of the light curve, which indicates that an effective χ^2 improvement due to the microlensing signal is negligibly small. We also examined the xallarap effect by simultaneously fitting it with the parallax parameters, but it changes neither the model nor the parallax vector much. We note that values of t_E and ρ are consistent between the parallax alone model and the parallax plus LOM/xallrap model.

Despite the strict constraint of the parallax parameters imposed by the simultaneous fitting of the parallax effect and LOM, we confirmed that the deviation around HJD′ ∼ 6760 is also explainable by the LOM or xallarap alone, which accepts null detection of the parallax. We thus conclude the parallax parameters cannot be determined contrary to the small model uncertainty.

There is also a large dispersion in the distribution of ρ as shown in Figure 6 where the posterior distributions of ρ are plotted. The dispersion is due to the sparsity of data points taken during the caustic entry and exit. The distributions are well characterized by the superposition of two Gaussian distributions, and the best-fit finite-source parameter of the models lies either of the bimodal peaks. This bimodal feature is associated with the uncertainty in ρ, causing it to be larger.

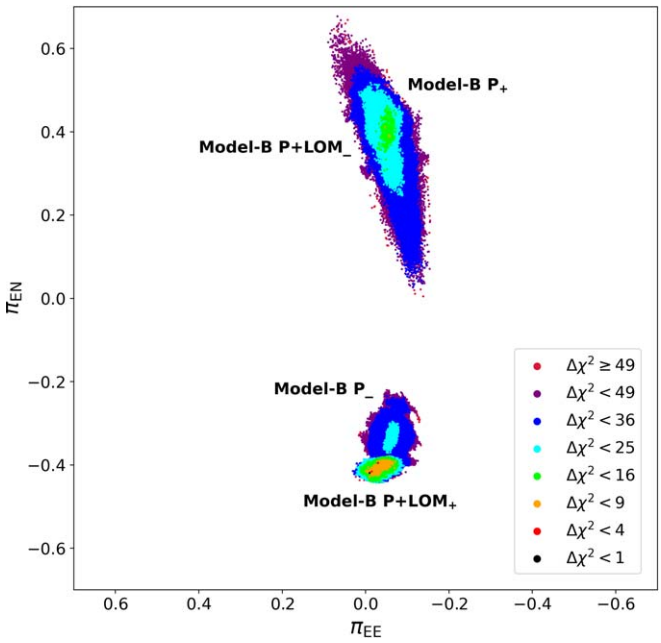

Figure 5. Posterior distribution sampled by the MCMC sampler. Colors represent $\Delta\chi^2$ from the lowest χ^2 parallax plus LOM model.

4. Source Property

Once the finite-source effect is detected, the angular Einstein radius $\theta_E = \frac{\theta_*}{\rho}$ can be determined by measuring the angular size of the source, and the relative proper motion $\mu_{rel} = \frac{\theta_E}{t_E}$ can also be estimated, combining with t_E measured from the light curve. An empirical relation of the angular source size as a function of the cousins I and V bands is derived based on the result of Boyajian et al. (2014). By restricting to stars with $3900\,K < T_{eff} < 7000\,K$, optimal to FGK stars, Fukui et al. (2015) finds:

$$\log[2\theta_*/\mathrm{mas}] = 0.5014 + 0.4197(V - I) - 0.2I. \quad (5)$$

We calibrated the source magnitude in the instrumental OGLE I and V bands to the standard Kron–Cousins and

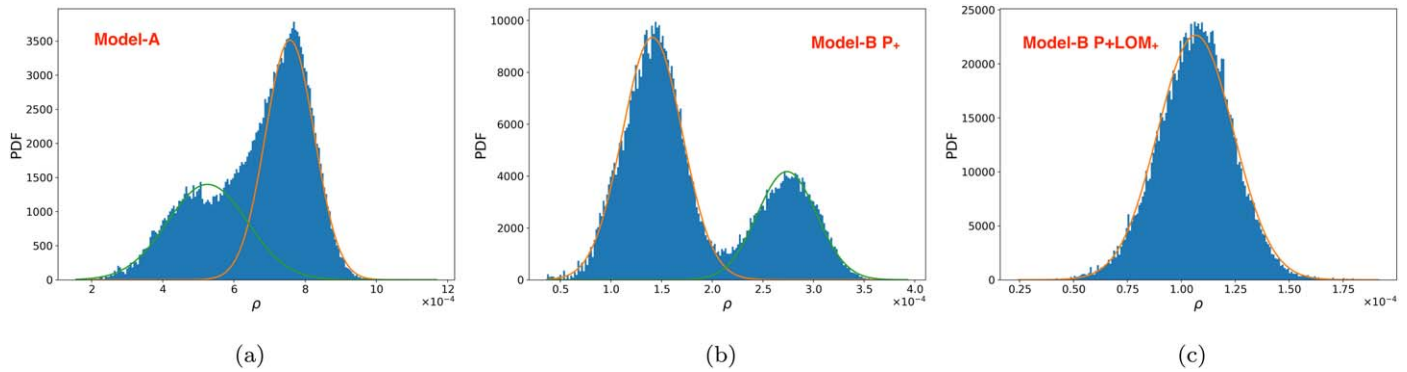

Figure 6. Probability density functions of the normalized angular source radius ρ from our MCMC chains for (a) Model-A, (b) Model-B P_+, and (c) Model-B P +LOM_+. The bimodal distribution of each model except Model-B P+LOM_+ is approximated by the Gaussian mixture model, and the two components of the best fit are plotted in orange and green lines.

Johnson system using the following equations from Udalski et al. (2015):

$$(V-I) = \mu \cdot [(v_{DB} + \Delta \mathrm{ZP}_V) - (i_{DB} + \Delta \mathrm{ZP}_I)]$$
$$I = (i_{DB} + \Delta \mathrm{ZP}_I) + \epsilon_I \cdot (V-I)$$
$$V = (v_{DB} + \Delta \mathrm{ZP}_V) + \epsilon_V \cdot (V-I), \quad (6)$$

where i_{DB} and v_{DB} are the instrumental I and V, $\mu = (1 - \epsilon_V + \epsilon_I)^{-1}$, $\Delta \mathrm{ZP}_I = 0.018$, $\Delta \mathrm{ZP}_V = 0.158$, $\epsilon_I = -0.005 \pm 0.003$, and $\epsilon_V = -0.077 \pm 0.001$ for the field of OGLE-2014-BLG-0221. The calibrated color and magnitude $(V-I,\ I)_{\mathrm{S}}$ are plotted onto the color–magnitude diagram (CMD) of the stars within 2′ of the event coordinate (Figure 7). The instrumental source magnitude is derived from the light curve by simultaneously fitting to the source and blending. While the instrumental I-band magnitude is well constrained, the instrumental V-band magnitude has a moderately large uncertainty due to fewer (∼20) data points in the magnification portion of the light curve.

The central color and magnitude of the red clump giants (RCGs) population marked in the CMD is representative of the bulge RCGs. We followed the standard procedure adopted in Yoo et al. (2004) to correct the effect of reddening and extinction due to interstellar dust, under the assumption that the source experiences the same reddening and extinction as the bulge RCGs. The centroid of the RCGs was $(V-I,\ I)_{\mathrm{RCG}} = (2.358,\ 15.947) \pm (0.009,\ 0.023)$ from the color–magnitude distribution, and the extinction-free color and magnitude of the bulge RCGs were known as $(V-I,\ I)_{\mathrm{RCG,\ 0}} = (1.060,\ 14.349) \pm (0.070,\ 0.040)$ toward the event coordinate (Bensby et al. 2011; Nataf et al. 2013), and for which the reddening and extinction were estimated as $(E(V-I),\ A(I)) = (1.298,\ 1.598) \pm (0.071,\ 0.046)$. Applying the same reddening and extinction and using the earlier empirical relation, we found the intrinsic color and magnitude of the source $(V-I,\ I)_{\mathrm{S,0}}$ and the angular source size θ_* for Model-A, Model-B P ± and Model-B P+LOM ±, which let us calculate θ_{E} and μ_{rel}. Those values are given in Table 4.

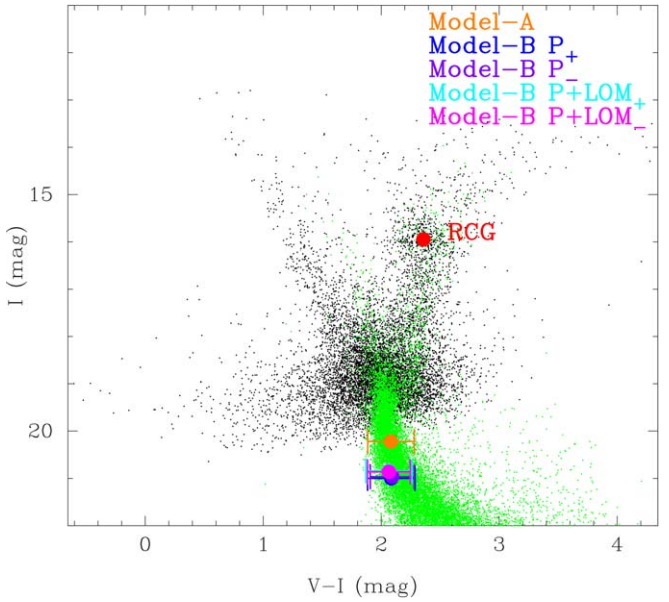

Figure 7. $(V-I,\ I)$ Color–magnitude diagram of stars in the OGLE-I I I catalog (Szymański et al. 2011) and the Hubble Space Telescope catalog (Holtzman et al. 1998). The black dots are the OGLE-I I I catalog stars located within 2′ of the event OGLE-2014-BLG-0221, and the green dots are the Hubble Space Telescope catalog stars in a field of Baade's window, whose colors and magnitudes are shifted to match the red clump giant centroid of the OGLE-I I I catalog. The red spot indicates the position of the red clump giant centroid, and the orange, blue, purple, cyan, and magenta spots are source positions of Model-A, Model-B P ±, and Model-B P+LOM ±, respectively.

5. Lens Properties

As parallax could not be measured accurately, we used a Bayesian approach to infer the lens physical properties. The microlensing event simulation code (Koshimoto & Ranc 2021) with a parametric Galactic model toward the Galactic bulge developed by Koshimoto et al. (2021) was used to generate artificial microlensing events and obtain posterior distributions of the physical parameters. The likelihood of the measured parameters, t_{E} and θ_{E}, was included as the observed constraints. An upper limit of the lens brightness was also set as $I_{\mathrm{lim}} = 18$ mag, determined based on the blending magnitude but about 2 mag brighter to make the analysis conservative. From the OGLE-I I I catalog, we also confirmed there is no potential source within 2″ of the event coordinate that is brighter than the limit. Apparent lens magnitudes of the simulated events were estimated using the mass–luminosity and color–color relations of main-sequence stars (Kroupa et al. 1993; Kenyon & Hartmann 1995) and the extinction law (Nishiyama et al. 2009). The following extinction model was assumed from

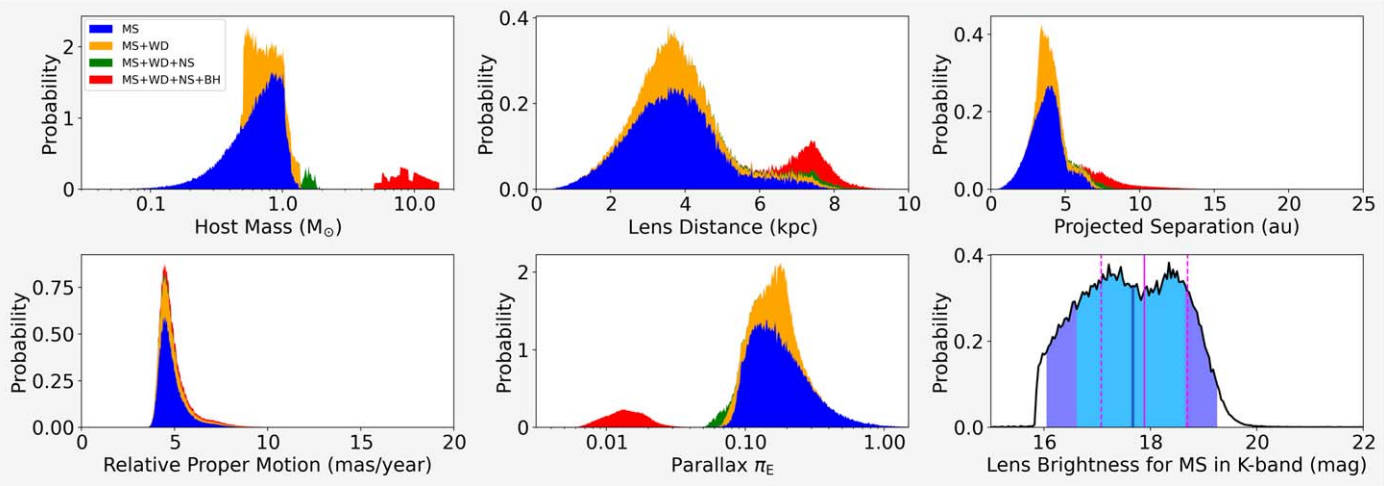

Figure 8. Posterior probability density distributions of Model-A. The distributions are classified into main-sequence stars, WDs, neutron stars, and BHs and are separated by colors accordingly. In the last plot, the lens brightness of the main-sequence samples is shown, where the vertical blue line is the median value and the cyan and purple regions represent 68.3% and 95.4% credible intervals of the distribution. The apparent source brightness is also plotted by the median magenta line with the magenta dashed line indicating the 68.3% interval.

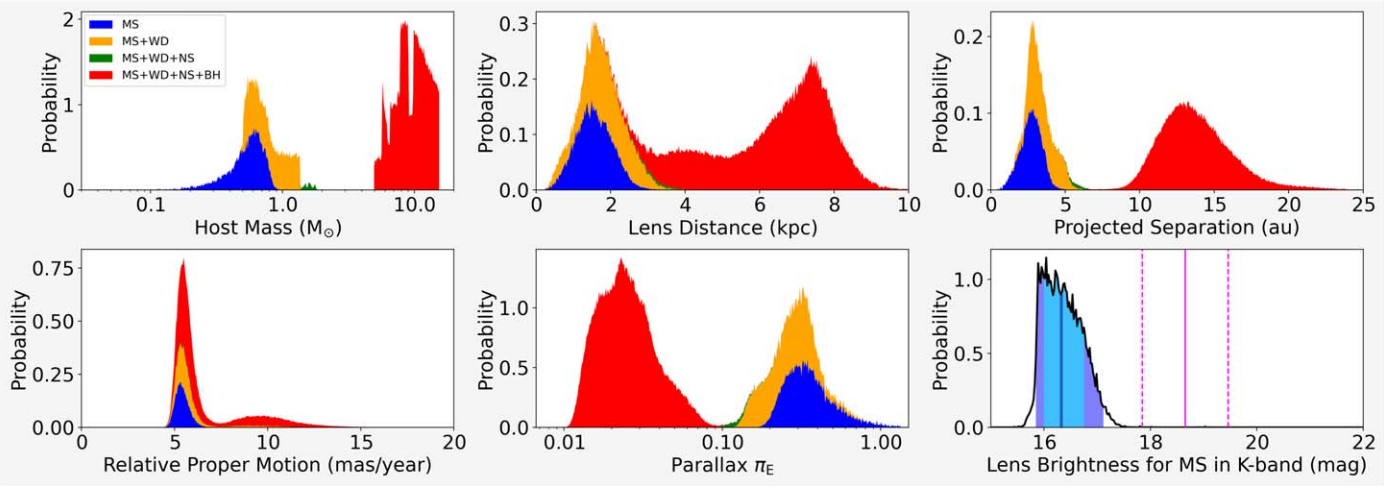

Figure 9. Same as Figure 8 for Model-B P_+.

Table 4
Source/Lens Properties

	Model-A	Model-B P_+	Model-B P_-	Model-B P+LOM$_+$	Model-B P+LOM$_-$
$(V-I, I)_S$	(2.082, 20.221)	(2.085, 20.998)	(2.093, 20.964)	(2.066, 20.842)	(2.065, 20.861)
	$\pm$(0.183, 0.028)	$\pm$(0.183, 0.033)	$\pm$(0.185, 0.046)	$\pm$(0.182, 0.035)	$\pm$(0.181, 0.017)
$(V-I, I)_{S,0}$	(0.784, 18.623)	(0.787, 19.400)	(0.795, 19.367)	(0.768, 19.244)	(0.767, 19.263)
	$\pm$(0.196, 0.054)	$\pm$(0.196, 0.057)	$\pm$(0.198, 0.065)	$\pm$(0.195, 0.058)	$\pm$(0.194, 0.049)
θ_* (μas)	0.638 ± 0.122	0.447 ± 0.085	0.457 ± 0.089	0.471 ± 0.090	0.467 ± 0.088
θ_E (mas)	0.82 ± 0.23	3.19 ± 1.86	3.19 ± 0.76	4.83 ± 1.25	4.20 ± 1.05
μ_{rel} (mas/year)	4.42 ± 1.22	10.77 ± 6.29	11.07 ± 2.65	16.08 ± 4.19	13.59 ± 3.42

Bennett et al. (2015) for the dependence on the lens distance,

$$A_L = \frac{1 - e^{-D_L \sin|b|/0.1\mathrm{kpc}}}{1 - e^{-D_{RC} \sin|b|/0.1\mathrm{kpc}}} A_{RC}, \quad (7)$$

where A_L is the extinction experienced by the lens and A_{RC} is the extinction of the bulge RCGs toward the event coordinate. The equation presumes dust in the foreground of the lens with a dust scale height of 0.1 kpc. In addition to a stellar luminous lens, we also generated a remnant dark lens in accordance with the PARSEC isochrone models (Bressan et al. 2012; Chen et al. 2014; Tang et al. 2014) of stellar evolution and the remnant initial-final mass relation (Lam et al. 2020) implemented in the

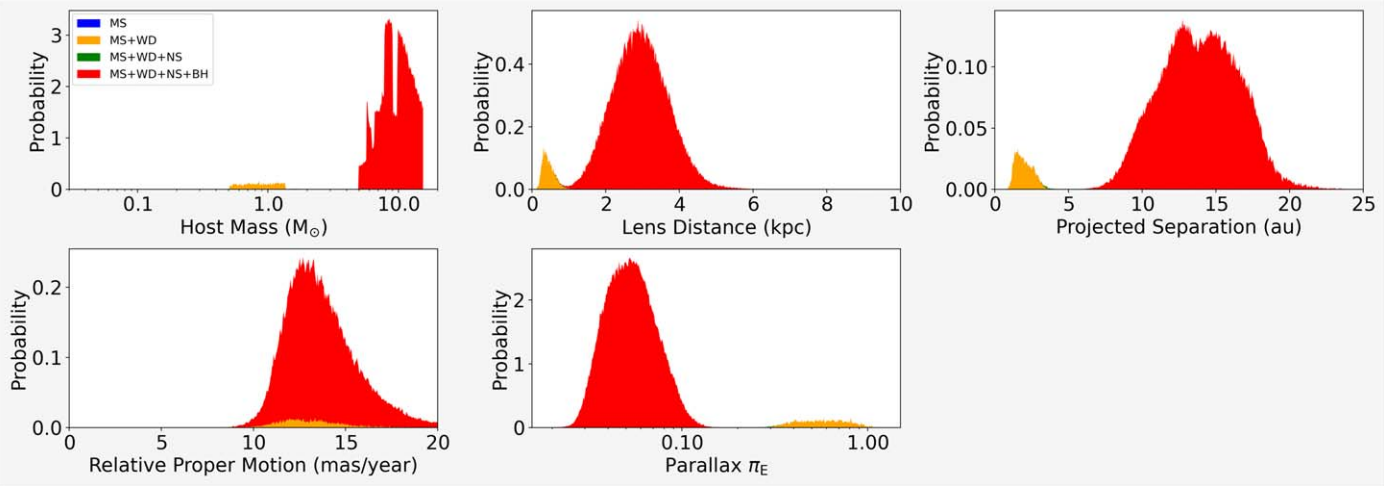

Figure 10. Same as Figure 8 for Model-B P+LOM$_+$. The plot of the lens brightness is not shown as no main-sequence sample has been generated in the simulation.

simulation code. Natal kick velocities of 350 and 100 km s^{-1} are assumed for neutron stars and BHs, respectively, following Lam et al. (2020).

Figures 8, 9, and 10 show the posterior probability density distributions of the physical parameters for Model-A, Model-B P$_+$, and Model-B P+LOM$_+$ with 10^6 simulated microlensing samples accepted under the constraints, and Table 5 lists the physical parameters. We did not simulate events for Model-B P$_-$ and Model-B P+LOM$_-$ as their likelihood and constraints on the Bayesian analysis are practically the same as those for Model-B P$_+$ and Model-B P+LOM$_+$, respectively.

The event simulation results assuming Model-A indicate that the lens system is most likely a planetary system consisting of a late-type star orbited by a gas giant. The simulation also generated remnant samples; WD lenses at almost identical parameter ranges as main-sequence lenses occupy ∼70% of the remnant distributions. A bimodal feature appears in the lens distance distribution because the prior probability is weighted more to the Galactic center region, whereas the model requires a nearby lens for a low-mass system, i.e., main-sequence and WD lenses, to explain the longer t_E and larger θ_E, which are proportional to the square root of $\pi_{rel} = (1\,\mathrm{au})(1/D_L - 1/D_S)$.

On the other hand, for Model-B, the result supports a conclusion that the lens system is most likely composed of a remnant orbited by a gas giant, brown dwarf, or red dwarf depending on the host mass, which is a reasonable consequence of the longer t_E and larger θ_E likelihood compared to that suggested by Model-A. In particular, it is notable that the predicted percentage of remnant lenses is 100% for Model-B P+LOM$_+$ with more than 95% of the distributions occupied by BH lenses. Discrepancies between the distributions of the Model-B P$_+$ and Model-B P+LOM$_+$ parameters as well as fractions in the lens types mostly come from the broad likelihood distribution of the Model-B P$_+$ parameters due to the dispersion in the finite-source effect parameter. The upper end of the main-sequence distributions is constrained by the upper limit imposed on the lens brightness.

6. Summary and Discussion

The results of the light-curve modeling and investigation of the source and lens properties are shown in the preceding sections. We found two degenerate models, Model-A and Model-B, that have similar companion parameter values of $q \sim 5 \times 10^{-3}$ and $s \sim 1.1$ but dissimilar microlensing parameter values of $t_E \sim (70, 110)$ days and $\rho \sim (5, 1) \times 10^{-4}$. Due to the long event timescale and large angular Einstein radius, both models favored a nearby heavy-lens solution; furthermore, a Bayesian analysis including remnant populations in the lens system prior revealed the lens to be a remnant candidate. We note that there is a crucial assumption that stars and stellar remnants possess equal probabilities of hosting companions with Jupiter mass ratios. Indeed, it might be uncommon for a system with such an extreme mass ratio to form around neutron stars and BHs (e.g., Martin et al. 2016).

6.1. Interpretation of the Lens System

Although several combinations of the host and companion object types are proposed regarding the posterior distributions as shown in Table 5, they can be divided roughly into three pairs, a gas giant planet with a main-sequence star, a gas giant with a remnant, and a brown dwarf or red dwarf with a BH.

Both close-in and distant giant planets around main-sequence stars are found to date by various survey techniques and statistically studied for their occurrence around different spectral types of hosts. For microlensing, Suzuki et al. (2018) compared the statistical analysis result of planet occurrence presented in Suzuki et al. (2016) to the core accretion model (Ida & Lin 2004; Mordasini et al. 2009) and confirmed excess in microlensing planets beyond $q \sim 10^{-4}$, including a factor ∼5 discrepancy for $10^{-3} < q \leqslant 0.03$. The favored value for q for event OGLE-2014-BLG-0221 will add to that discrepancy. The MOA collaboration is preparing an extended analysis of Suzuki et al. (2016) with extended data beyond 2007–2012 in which OGLE-2014-BLG-0221 will be included. There is other observational evidence from various observational methods that support some modification to the traditional planet formation scenarios of giant planets. A recent study of transiting planets discovered by TESS indicates a higher occurrence rate of giant planets around low-mass stars than the rate predicted by the core accretion model (Bryant et al. 2023). The discovery of four distant giant planets around HR 8799 by direct imaging suggests that gravitational instability (Boss 1997) would play an important role in planet formation (Marois et al. 2008, 2010).

Table 5
Estimated Lens Physical Parameters from the Bayesian Analysis

		Model-A	Model-B P_+	Model-B P+LOM$_+$
Main-sequence Host	Companion Mass $M_{\rm comp}$ ($M_{\rm jup}$)	$4.35^{+1.65}_{-1.91}$	$4.13^{+1.04}_{-1.28}$	—
	Host Mass $M_{\rm host}$ ($M_\odot$)	$0.69^{+0.26}_{-0.30}$	$0.57^{+0.14}_{-0.18}$	—
	Projected Separation $a_\perp$ (au)	$3.76^{+0.96}_{-1.07}$	$2.75^{+0.65}_{-0.76}$	—
	Lens Distance $D_{\rm L}$ (kpc)	$3.68^{+1.13}_{-1.16}$	$1.56^{+0.51}_{-0.50}$	—
	Source Distance $D_{\rm S}$ (kpc)	$7.97^{+2.51}_{-0.70}$	$7.87^{+1.27}_{-0.71}$	—
	Angular Einstein Radius $\theta_{\rm E}$ (mas)	$0.87^{+0.14}_{-0.08}$	$1.52^{+0.13}_{-0.11}$	—
	Relative Proper Motion $\mu_{\rm rel}$ (mas/year)	$4.67^{+0.76}_{-0.37}$	$5.41^{+0.43}_{-0.30}$	—
	Parallax $\pi_{\rm E}$	$0.171^{+0.110}_{-0.048}$	$0.351^{+0.156}_{-0.093}$	—
	Lens Brightness in V Band $V_{\rm L}$ (mag)	$22.9^{+2.2}_{-1.8}$	$21.5^{+0.8}_{-0.9}$	—
	Lens Brightness in I Band $I_{\rm L}$ (mag)	$20.4^{+1.4}_{-1.3}$	$18.9^{+0.6}_{-0.5}$	—
	Lens Brightness in H Band $H_{\rm L}$ (mag)	$17.9^{+1.1}_{-1.1}$	$16.7^{+0.4}_{-0.4}$	—
	Lens Brightness in K Band $K_{\rm L}$ (mag)	$17.7^{+1.0}_{-1.1}$	$16.3^{+0.4}_{-0.3}$	—
	Source Brightness in V Band $V_{\rm S}$ (mag)	22.30 ± 0.18	23.08 ± 0.18	22.90 ± 0.18
	Source Brightness in I Band $I_{\rm S}$ (mag)	20.22 ± 0.03	21.00 ± 0.03	20.84 ± 0.04
	Source Brightness in H- Bnd $H_{\rm S}$ (mag)	18.1 ± 0.8	18.9 ± 0.8	18.8 ± 1.2
	Source Brightness in K Band $K_{\rm S}$ (mag)	17.9 ± 0.8	18.7 ± 0.8	18.6 ± 1.2
	Fraction of the Sample	64.8%	18.0%	—
WD Host	Companion Mass $M_{\rm comp}$ ($M_{\rm jup}$)	$4.23^{+2.30}_{-0.76}$	$5.68^{+2.51}_{-1.50}$	$4.29^{+1.61}_{-1.27}$
	Host Mass $M_{\rm host}$ ($M_\odot$)	$0.67^{+0.36}_{-0.12}$	$0.78^{+0.34}_{-0.21}$	$0.87^{+0.32}_{-0.26}$
	Projected Separation $a_\perp$ (au)	$3.83^{+1.05}_{-0.49}$	$3.34^{+1.21}_{-0.71}$	$1.87^{+0.68}_{-0.48}$
	Lens Distance $D_{\rm L}$ (kpc)	$3.75^{+1.19}_{-0.76}$	$1.85^{+0.69}_{-0.53}$	$0.42^{+0.21}_{-0.11}$
	Source Distance $D_{\rm S}$ (kpc)	$8.04^{+3.41}_{-0.79}$	$7.84^{+1.12}_{-0.70}$	$7.78^{+1.03}_{-0.80}$
	Angular Einstein Radius $\theta_{\rm E}$ (mas)	$0.87^{+0.16}_{-0.08}$	$1.60^{+0.28}_{-0.13}$	$3.95^{+0.57}_{-0.47}$
	Relative Proper Motion $\mu_{\rm rel}$ (mas/year)	$4.69^{+0.89}_{-0.40}$	$5.64^{+0.69}_{-0.43}$	$12.91^{+1.94}_{-1.39}$
	Parallax $\pi_{\rm E}$	$0.171^{+0.034}_{-0.070}$	$0.266^{+0.103}_{-0.090}$	$0.576^{+0.226}_{-0.164}$
	Fraction of the Sample	24.7%	20.8%	4.3%
Neutron Star Host	Companion Mass $M_{\rm comp}$ ($M_{\rm jup}$)	$10.15^{+0.73}_{-0.82}$	$11.75^{+0.90}_{-1.15}$	$7.89^{+0.76}_{-0.45}$
	Host Mass $M_{\rm host}$ ($M_\odot$)	$1.61^{+0.11}_{-0.13}$	$1.61^{+0.12}_{-0.16}$	$1.59^{+0.15}_{-0.09}$
	Projected Separation $a_\perp$ (au)	$7.12^{+0.68}_{-1.46}$	$5.71^{+0.50}_{-0.53}$	$3.38^{+0.45}_{-0.29}$
	Lens Distance $D_{\rm L}$ (kpc)	$7.23^{+0.66}_{-1.75}$	$3.15^{+0.44}_{-0.60}$	$0.77^{+0.29}_{-0.11}$
	Source Distance $D_{\rm S}$ (kpc)	$12.20^{+2.04}_{-3.89}$	$8.02^{+1.79}_{-0.72}$	$7.81^{+0.98}_{-0.61}$
	Angular Einstein Radius $\theta_{\rm E}$ (mas)	$0.86^{+0.10}_{-0.07}$	$1.60^{+0.22}_{-0.14}$	$3.86^{+0.45}_{-0.51}$
	Relative Proper Motion $\mu_{\rm rel}$ (mas/year)	$4.61^{+0.54}_{-0.34}$	$5.63^{+0.67}_{-0.44}$	$12.61^{+1.49}_{-1.51}$
	Parallax $\pi_{\rm E}$	$0.065^{+0.013}_{-0.008}$	$0.121^{+0.030}_{-0.002}$	$0.051^{+0.031}_{-0.003}$
	Fraction of the Sample	2.0%	0.6%	0.1%
BH Host	Companion Mass $M_{\rm comp}$ ($M_{\rm jup}$)	$55.00^{+22.73}_{-14.91}$	$72.16^{+24.50}_{-21.84}$	$48.62^{+15.60}_{-13.62}$
	Host Mass $M_{\rm host}$ ($M_\odot$)	$8.71^{+3.60}_{-2.36}$	$9.90^{+3.36}_{-3.00}$	$9.81^{+3.15}_{-2.75}$
	Projected Separation $a_\perp$ (au)	$8.17^{+2.37}_{-1.04}$	$13.52^{+2.54}_{-1.99}$	$13.30^{+2.69}_{-2.61}$
	Lens Distance $D_{\rm L}$ (kpc)	$7.45^{+0.52}_{-0.52}$	$6.75^{+1.04}_{-2.45}$	$2.94^{+0.78}_{-0.75}$
	Source Distance $D_{\rm S}$ (kpc)	$8.30^{+0.81}_{-0.59}$	$8.87^{+2.69}_{-1.18}$	$7.97^{+1.14}_{-0.65}$
	Angular Einstein Radius $\theta_{\rm E}$ (mas)	$0.94^{+0.32}_{-0.12}$	$1.73^{+1.18}_{-0.22}$	$4.10^{+0.65}_{-0.47}$
	Relative Proper Motion $\mu_{\rm rel}$ (mas/year)	$5.05^{+1.75}_{-0.59}$	$5.95^{+3.94}_{-0.58}$	$13.48^{+2.16}_{-1.57}$
	Parallax $\pi_{\rm E}$	$0.015^{+0.016}_{-0.006}$	$0.025^{+0.021}_{-0.008}$	$0.051^{+0.031}_{-0.003}$
	Fraction of the Sample	8.3%	60.6%	95.6%

There are a few cases of exoplanets discovered around a WD or a neutron star, including the first exoplanets detected in 1992 around a pulsar, PSR B1257 + 12 (Wolszczan & Frail 1992). However, most of them represent extreme environments; for example, PSR B1620-26AB b is a circumbinary planet around a pulsar–WD binary (Thorsett et al. 1993; Sigurdsson et al. 2003), WD 0806-661 b has a very large separation of 2500 au from its host (Luhman et al. 2011), and WD1856 + 534 b has a small separation of 0.02 au (Vanderburg et al. 2020). Only MOA-2010-BLG-477Lb is a currently known planet orbiting about a few au away from a WD (Blackman et al. 2021). It is still uncertain how a solar-analogous planetary system evolves along with its host star. Several mechanisms are proposed such as common envelopes during the giant phase (Paczynski 1976) that result in short planetary orbits or stellar mass loss that pushes planets outward (Veras 2016). Second-generation exoplanets, those formed during the post-main-sequence phase, are also proposed as an alternative scenario for some of the observed systems (Perets 2010; Ledda et al. 2023). Despite the importance of finding more observational samples, observational bias hinders the solid detection of a WD planetary system. The low luminosity of WDs makes astrometry and transit monitoring difficult, the noncharacteristic features of a WD spectrum prevent measuring radial velocity, and direct

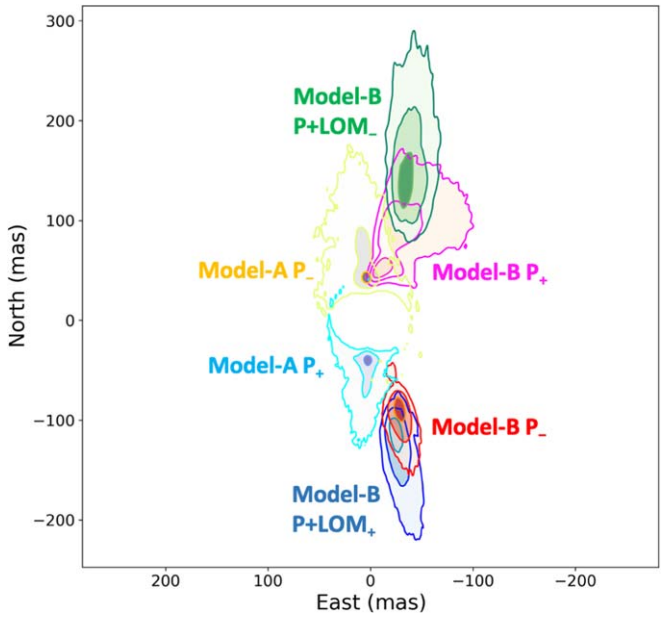

Figure 11. Current source–lens relative position. The distributions of Model-A $P_{\pm}$, Model-B $P_{\pm}$, and Model-B P+LOM$_{\pm}$ are plotted. The contour from dark to light shows 39.3, 86.5, and 98.9% of the highest-density regions.

imaging is biased toward wide orbits as WD 0806-661 b shows. In contrast, microlensing has an advantage as it does not rely on the host star brightness, and a microlensing survey toward the Galactic center has a peak sensitivity of planet–host separation at a few au, which is suitable for filling the gap between close-in to distant planets around WDs. If the OGLE-2014-BLG-0221 system has a WD host, an analogous system to MOA-2010-BLG-477 is expected. This would provide us with insight into potential planetary survival scenarios within the few au separation range.

Microlensing can also detect a planet around an X-ray quiet neutron star with its capability of finding dark objects that is not achievable by any other method. Although the pulsar timing method is the only method successful to date for detecting a planet around a neutron star,[20] microlensing would shed light on a cold planet around an unseen neutron star if the host of OGLE-2014-BLG-0221 is a neutron star.

More than a dozen stellar mass BH binaries are known but are mostly found by light from X-ray binaries where the accretion of material from a companion occurs and is therefore a closely packed system (e.g., Corral-Santana et al. 2016). A few noninteracting BH candidates are also identified by radial velocity (e.g., Mahy et al. 2022; Shenar et al. 2022) and astrometry (Chakrabarti et al. 2023; El-Badry et al. 2023), in which $\sim$1.4 au is the widest orbital separation between the candidate and its companion. Several population synthesis studies predict that large fractions of BH luminous companion binaries should have a wide separation such that the orbital period becomes more than years (e.g., Chawla et al. 2022), much longer than any of the confirmed candidates. We estimated that OGLE-2014-BLG-0221 has a projected separation of $\sim$10 au for the case of a BH host; thus, it would represent the longest BH binary separation ever known and belong to the theoretically predicted population of wide orbit BH binaries. Moreover, the companion is supposed to be a very low-mass star or a brown dwarf, and in either case is too faint to be detected by photometry, indicating such a system is unlikely found by any other method besides microlensing.

[20] Seven planets are confirmed including three planets belonging to the PSR B1257 + 12 system (Akeson et al. 2013).

6.2. Future Follow-up Observation

Future deep optical imaging is valuable for disentangling the luminous and dark lens scenarios in this event. As the source brightness in the *I* band is well constrained from the light-curve modeling, measurement of the total flux in a similar wavelength would provide strong constraints on the model probabilities. Especially if no object with $20.3 > I$ is confirmed, Model-A will be ruled out, and only the dark lens scenarios of Model-B P_+ and Model-B P+LOM$_+$ will survive, leading to the conclusion that OGLE-2014-BLG-0221 is a remnant system.

Once the source and lens are separated enough following their proper motions after several years of the event peak, we would be able to resolve the source and lens with high-resolution imaging (e.g., Hubble Space Telescope, Keck adaptive optics). This idea was first developed by Bennett et al. (2006, 2007), and the number of identifications has increased in recent years (e.g., Bennett et al. 2015; Bhattacharya et al. 2018; Terry et al. 2021). Measurement of the lens–source separation and the lens brightness allows strong constraints to be placed on the mass–distance relation of the lens. Here, we consider the detectability of the lens using the future high-resolution imaging of OGLE-2014-BLG-0221.

Figure 11 is the posterior distribution of the predicted source–lens separation for each degenerate model with the parallax parameters included, derived from the MCMC parameter chains. The separation is computed from the heliocentric proper motion vector:

$$\mu_{\rm rel,\ hel} = \mu_{\rm rel}\hat{\pi}_{\rm E} + v_{\oplus}\frac{\pi_{\rm rel}}{\rm au}, \tag{8}$$

where $\hat{\pi}_{\rm E}$ is the unit vector of the microlensing parallax and $v_{\oplus}$ is the Earth's projected velocity at t_0. While the direction of the separation is largely dependent on the microlensing parallax vector, the conversion from the geocentric to the heliocentric reference frame does not change the separation itself much unless the relative parallax is too large. We estimated the current separation is 41 ± 7 and 45 ± 14 mas for Model-A $P_{\pm}$, 103 ± 28 and 98 ± 13 mas for Model-B $P_{\pm}$, and 139 ± 20 and 132 ± 28 mas for Model-B P+LOM$_{\pm}$, respectively. Hence, we expect the source and lens to be separated enough to conduct high-resolution imaging; otherwise, the separation is unexpectedly small owing to its uncertainty. By measuring the current position, we would discriminate the models as the direction and magnitude of the separation are likely different among the models. The large expected source–lens separation of Model-B would be due to the small lens distance or the kick velocity caused when an NS or BH forms as discussed in Lam et al. (2020).

The relative source–lens brightness is also a major concern when resolving the source and lens. Similar brightness is preferred to identify both source and lens; however, Bhattacharya et al. (2021) demonstrated that the lens can be identified even if it is a few magnitudes fainter than the source. For the case of OGLE-2014-BLG-0221, photometric detection of the lens indicates that the system most likely follows Model-A. From the Bayesian posterior distribution, we obtained the

estimation of the apparent lens magnitude $(I_L, H_L) = (20.4^{+1.4}_{-1.3}, 17.9^{+1.1}_{-1.1})$ for Model-A. This should be luminous enough as, for example, Blackman et al. (2021) determined the detection limit of their high-resolution Keck image as 21.1 mag in the H band. In comparison to the lens brightness, a similar apparent source magnitude is expected from the modeling as $(I_S, H_S) = (20.22, 18.1) \pm (0.03, 0.8)$ for Model-A, making the event ideal for high-resolution imaging. Furthermore, Model-B measures the different apparent source magnitude $(I_S, H_S) = (21.00, 18.9) \pm (0.03, 0.8)$ and $(20.84, 18.8) \pm (0.04, 1.2)$ for Model-B P_+ and Model-B P+LOM$_+$, from that of Model-A. This indicates the model degeneracy would be disentangled with observations of the source even though the lens is not observable for the case of a remnant lens. I-band high-resolution imaging with the Hubble Space Telescope is best suited for this purpose because the source brightness has been precisely measured in the I band. It should resolve all the degeneracies, whether luminous or dark lens, and whether Model-A or Model-B.

Finally, if precise astrometric measurements are conducted in multiple bands, the color-dependent centroid shift (Bennett et al. 2006) may be detected in the luminous lens scenario. This refers to the change in the blended point-spread function centroid depending on the wavelength, caused by differences in colors between the source and lens. As the centroid can generally be measured with much better accuracy than spatial resolution, color-dependent centroid shift may be measured even when the source and lens are not spatially resolved. Hence, future follow-up observations are highly important for characterizing OGLE-2014-BLG-0221.

Acknowledgments

We appreciate Iona Kondo and Kento Masuda for the valuable comments and discussions. We would also like to thank the anonymous referee for the positive attitude and suggestions. The MOA project is supported by JSPS KAKENHI grant Nos. JP24253004, JP26247023, JP16H06287, and JP22H00153. R.K. was supported by JST SPRING, grant No. JPMJSP2138. D.P.B. acknowledges support from NASA grants 80NSSC20K0886 and 80NSSC18K0793. D.S. was supported by JSPS KAKENHI grant No. 19KK0082. This work was supported by the JSPS Core-to-Core Program (grant No.: JPJSCCA20210003). N.K. was supported by the JSPS overseas research fellowship.

ORCID iDs

Rintaro Kirikawa https://orcid.org/0009-0005-3016-4211
Takahiro Sumi https://orcid.org/0000-0002-4035-5012
David P. Bennett https://orcid.org/0000-0001-8043-8413
Daisuke Suzuki https://orcid.org/0000-0002-5843-9433
Naoki Koshimoto https://orcid.org/0000-0003-2302-9562
Shota Miyazaki https://orcid.org/0000-0001-9818-1513
Andrzej Udalski https://orcid.org/0000-0001-5207-5619
Nicholas J. Rattenbury https://orcid.org/0000-0001-5069-319X
Richard Barry https://orcid.org/0000-0003-4916-0892
Akihiko Fukui https://orcid.org/0000-0002-4909-5763
Yuki Hirao https://orcid.org/0000-0003-4776-8618
Stela Ishitani Silva https://orcid.org/0000-0003-2267-1246
Yoshitaka Itow https://orcid.org/0000-0002-8198-1968
Yutaka Matsubara https://orcid.org/0000-0002-9629-4810
Yasushi Muraki https://orcid.org/0000-0003-1978-2092
Greg Olmschenk https://orcid.org/0000-0001-8472-2219
Clément Ranc https://orcid.org/0000-0003-2388-4534
Yuki K. Satoh https://orcid.org/0000-0002-1228-4122
Radosław Poleski https://orcid.org/0000-0002-9245-6368
Jan Skowron https://orcid.org/0000-0002-2335-1730
Michał K. Szymański https://orcid.org/0000-0002-0548-8995
Igor Soszyński https://orcid.org/0000-0002-7777-0842
Paweł Pietrukowicz https://orcid.org/0000-0002-2339-5899
Szymon Kozłowski https://orcid.org/0000-0003-4084-880X
Krzysztof Ulaczyk https://orcid.org/0000-0001-6364-408X

References

Akeson, R. L., Chen, X., Ciardi, D., et al. 2013, PASP, 125, 989
Alard, C., & Lupton, R. H. 1998, ApJ, 503, 325
Bachelet, E., Shin, I. G., Han, C., et al. 2012, ApJ, 754, 73
Bennett, D. P., Anderson, J., Bond, I. A., Udalski, A., & Gould, A. 2006, ApJL, 647, L171
Bennett, D. P., Anderson, J., & Gaudi, B. S. 2007, ApJ, 660, 781
Bennett, D. P., Bhattacharya, A., Anderson, J., et al. 2015, ApJ, 808, 169
Bennett, D. P., Bond, I. A., Udalski, A., et al. 2008, ApJ, 684, 663
Bennett, D. P., & Rhie, S. H. 1996, ApJ, 472, 660
Bensby, T., Adén, D., Meléndez, J., et al. 2011, A&A, 533, A134
Bhattacharya, A., Beaulieu, J. P., Bennett, D. P., et al. 2018, AJ, 156, 289
Bhattacharya, A., Bennett, D. P., Beaulieu, J. P., et al. 2021, AJ, 162, 60
Blackman, J. W., Beaulieu, J. P., Bennett, D. P., et al. 2021, Natur, 598, 272
Bond, I. A., Abe, F., Dodd, R. J., et al. 2001, MNRAS, 327, 868
Bond, I. A., Udalski, A., Jaroszyński, M., et al. 2004, ApJL, 606, L155
Boss, A. P. 1997, Sci, 276, 1836
Boyajian, T. S., van Belle, G., & von Braun, K. 2014, AJ, 147, 47
Bressan, A., Marigo, P., Girardi, L., et al. 2012, MNRAS, 427, 127
Bryant, E. M., Bayliss, D., & Van Eylen, V. 2023, MNRAS, 521, 3663
Burn, R., Schlecker, M., Mordasini, C., et al. 2021, A&A, 656, A72
Chakrabarti, S., Simon, J. D., Craig, P. A., et al. 2023, AJ, 166, 6
Chawla, C., Chatterjee, S., Breivik, K., et al. 2022, ApJ, 931, 107
Chen, Y., Girardi, L., bressan, A., et al. 2014, MNRAS, 444, 2525
Claret, A., & Bloemen, S. 2011, A&A, 529, A75
Corral-Santana, J. M., Casares, J., Muñoz-Darias, T., et al. 2016, A&A, 587, A61
Dong, S., Gould, A., Udalski, A., et al. 2009, ApJ, 695, 970
El-Badry, K., Rix, H.-W., Quataert, E., et al. 2023, MNRAS, 518, 1057
Fukui, A., Gould, A., Sumi, T., et al. 2015, ApJ, 809, 74
Gould, A. 2004, ApJ, 606, 319
Holtzman, J. A., Watson, A. M., Baum, W. A., et al. 1998, AJ, 115, 1946
Ida, S., & Lin, D. N. C. 2004, ApJ, 604, 388
Ida, S., & Lin, D. N. C. 2005, ApJ, 626, 1045
Kenyon, S. J., & Hartmann, L. 1995, ApJS, 101, 117
Koshimoto, N., Baba, J., & Bennett, D. P. 2021, ApJ, 917, 78
Koshimoto, N., & Ranc, C. 2021, nkoshimoto/genulens: a Tool for Gravitational Microlensing Events Simulation, v1.0, Zenodo, doi:10.5281/zenodo.4784949
Kroupa, P., Tout, C. A., & Gilmore, G. 1993, MNRAS, 262, 545
Lam, C. Y., Abrams, N., Andrews, J., et al. 2023, arXiv:2306.12514
Lam, C. Y., Lu, J. R., Hosek, M. W. J., Dawson, W. A., & Golovich, N. R. 2020, ApJ, 889, 31
Lam, C. Y., Lu, J. R., Udalski, A., et al. 2022, ApJL, 933, L23
Ledda, S., Danielski, C., & Turrini, D. 2023, A&A, 675, A184
Luhman, K. L., Burgasser, A. J., & Bochanski, J. J. 2011, ApJL, 730, L9
Mahy, L., Sana, H., Shenar, T., et al. 2022, A&A, 664, A159
Marois, C., Macintosh, B., Barman, T., et al. 2008, Sci, 322, 1348
Marois, C., Zuckerman, B., Konopacky, Q. M., Macintosh, B., & Barman, T. 2010, Natur, 468, 1080
Martin, R. G., Livio, M., & Palaniswamy, D. 2016, ApJ, 832, 122
Miyake, N., Udalski, A., Sumi, T., et al. 2012, ApJ, 752, 82
Mordasini, C., Alibert, Y., & Benz, W. 2009, A&A, 501, 1139
Mróz, P., Udalski, A., & Gould, A. 2022, ApJL, 937, L24
Mróz, P., Udalski, A., Skowron, J., et al. 2019, ApJS, 244, 29
Nataf, D. M., Gould, A., Fouqué, P., et al. 2013, ApJ, 769, 88
Nishiyama, S., Tamura, M., Hatano, H., et al. 2009, ApJ, 696, 1407

Paczynski, B. 1976, in IAU Symp. 73, Structure and Evolution of Close Binary Systems, ed. P. Eggleton, S. Mitton, & J. Whelan (Dordrecht: Reidel), 75
Paczynski, B. 1986, ApJ, 304, 1
Perets, H. B. 2010, arXiv:1001.0581
Poindexter, S., Afonso, C., Bennett, D. P., et al. 2005, ApJ, 633, 914
Sahu, K. C., Anderson, J., Casertano, S., et al. 2022, ApJ, 933, 83
Sako, T., Sekiguchi, T., Sasaki, M., et al. 2008, ExA, 22, 51
Shenar, T., Sana, H., Mahy, L., et al. 2022, NatAs, 6, 1085
Shvartzvald, Y., Udalski, A., Gould, A., et al. 2015, ApJ, 814, 111
Sigurdsson, S., Richer, H. B., Hansen, B. M., Stairs, I. H., & Thorsett, S. E. 2003, Sci, 301, 193
Skowron, J., Udalski, A., Gould, A., et al. 2011, ApJ, 738, 87
Spergel, D., Gehrels, N., Baltay, C., et al. 2015, arXiv:1503.03757
Sumi, T., Abe, F., Bond, I. A., et al. 2003, ApJ, 591, 204
Sumi, T., Bennett, D. P., Bond, I. A., et al. 2010, ApJ, 710, 1641
Suzuki, D., Bennett, D. P., Ida, S., et al. 2018, ApJL, 869, L34
Suzuki, D., Bennett, D. P., Sumi, T., et al. 2016, ApJ, 833, 145
Szymański, M. K., Udalski, A., Soszyński, I., et al. 2011, AcA, 61, 83
Tang, J., Bressan, A., Rosenfield, P., et al. 2014, MNRAS, 445, 4287
Terry, S. K., Bhattacharya, A., Bennett, D. P., et al. 2021, AJ, 161, 54
Thorsett, S. E., Arzoumanian, Z., & Taylor, J. H. 1993, ApJL, 412, L33
Udalski, A. 2003, AcA, 53, 291
Udalski, A., Szymański, M. K., & Szymański, G. 2015, AcA, 65, 1
Vanderburg, A., Rappaport, S. A., Xu, S., et al. 2020, Natur, 585, 363
Veras, D. 2016, RSOS, 3, 150571
Verde, L., Peiris, H. V., Spergel, D. N., et al. 2003, ApJS, 148, 195
Wolszczan, A., & Frail, D. A. 1992, Natur, 355, 145
Yee, J. C., Shvartzvald, Y., Gal-Yam, A., et al. 2012, ApJ, 755, 102
Yoo, J., DePoy, D. L., Gal-Yam, A., et al. 2004, ApJ, 603, 139